Article:

A statistical study of the metallicity of core-collapse supernovae based on VLT/MUSE integral-field-unit spectroscopy

Qiang Xi,[1,2] Ning-Chen Sun,[1,2,3]★ Yi-Han Zhao,[1,2] Justyn R. Maund [ORCID],[4] Zexi Niu,[1,2] Adam J. Singleton[5] and Jifeng Liu[1,2,3,6]

[1]*School of Astronomy and Space Science, University of Chinese Academy of Sciences, Beijing 100049, China*
[2]*National Astronomical Observatories, Chinese Academy of Sciences, Beijing 100101, China*
[3]*Institute for Frontiers in Astronomy and Astrophysics, Beijing Normal University, Beijing 102206, China*
[4]*Department of Physics, Royal Holloway, University of London, Egham TW20 0EX, UK*
[5]*School of Mathematical and Physical Sciences, University of Sheffield, Hicks Building, Hounsfield Road, Sheffield S3 7RH, UK*
[6]*New Cornerstone Science Laboratory, National Astronomical Observatories, Chinese Academy of Sciences, Beijing 100012, China*

ABSTRACT

Metallicity plays a crucial role in the evolution of massive stars and their final core-collapse supernova (CCSN) explosions. Integral-field-unit (IFU) spectroscopy can provide a spatially resolved view of SN host galaxies and serve as a powerful tool to study SN metallicities. While early transient surveys targeted high star formation rate and metallicity galaxies, recent untargeted, wide-field surveys (e.g. ASAS-SN, ZTF) have discovered large numbers of SNe without this bias. In this work, we construct a large sample of SNe discovered by wide-field untargeted searches, consisting of 161 SNe of Types II(P), IIn, IIb, Ib and Ic at $z \leq 0.02$ using observations carried out by the Multi-Unit Spectroscopic Explorer on the Very Large Telescope. This is currently the largest CCSN sample with IFU observations. With the strong-line method, we reveal the spatially resolved metallicity maps of the SN host galaxies and acquire accurate metallicity measurements for the SN sites, finding a range $12 + \log(O/H) = 8.1$–8.7 dex. Also, the metallicity distributions for different SN types are very close to each other, with mean and median values of 8.4–8.5 dex. Our large sample size narrows the 1σ uncertainty down to only 0.05 dex. The apparent metallicity differences among SN types are all within $\sim 1\sigma$ uncertainties and the metallicity distributions for different SN types are all consistent with being randomly drawn from the same reference distribution. This suggests that metallicity plays a minor role in the origin of different CCSN types, and that some other metallicity-insensitive processes, such as binary interaction, dominate the distinction of CCSN types.

Key words: stars: mass-loss – supernovae: general.

1 INTRODUCTION

Supernovae (SNe) are one of the most energetic catastrophic events in the Universe. They are categorized into Type I and Type II based on the presence of hydrogen lines in their spectra (Minkowski 1941). Other than the thermonuclear Type Ia SNe, the other types originate from the core collapse (CC) of massive stars with initial masses of $\gtrsim 8\,M_\odot$ (Bethe et al. 1979; Woosley & Weaver 1986; Arnett et al. 1989). Most hydrogen-rich SNe are of Type IIP, characterized by a plateau phase, powered by hydrogen recombination, in the light curve (Barbon, Ciatti & Rosino 1979). A fraction of SNe, classified as Type IIn, exhibit narrow emission lines in their spectra, arising from the strong interaction between the fast SN ejecta and slow circumstellar material (CSM; Schlegel 1990). Type Ib and Type Ic SNe are characterized by the absence of hydrogen features in their spectra, with Type Ic SNe also lacking helium features (Filippenko

1997). As an intermediate class between the hydrogen-rich and hydrogen-poor SNe, Type IIb displays hydrogen lines in the early phases of the explosion, resembling Type II, but these features disappear quickly in the later stages, appearing similar to Type Ib (Nomoto et al. 1993). For Types IIb, Ib and Ic, the disappearance or lack of hydrogen/helium features are due to the stripping of the outer envelopes of their progenitor stars. Therefore, they are also known as stripped-envelope (SE) SNe.

It is a major goal, and currently a major difficulty, to determine the progenitor stars of different types of SNe. Current research suggests that the progenitors of Type IIP SNe are red supergiants (RSGs) with massive hydrogen envelopes (Smartt 2009). However, stellar evolutionary theories are inconsistent with the lack of detection of high-mass (>16–$18\,M_\odot$) RSG progenitors (i.e. the 'RSG problem'; Smartt 2009). This could result from CSM extinction underestimating the mass of the RSG progenitor (Walmswell & Eldridge 2012; Beasor, Smith & Jencson 2025) or from high-mass RSGs collapsing directly into black holes without an SN (Kochanek 2014). It is also unclear

to what extent binary interactions dominate rather than contribute to the observed transient diversity (Zapartas et al. 2021; Bostroem et al. 2023).

While luminous blue variables (LBVs) have been proposed as Type IIn SN progenitors (Gal-Yam et al. 2007; Kiewe et al. 2012; Smith 2014; Elias-Rosa et al. 2016; Niu, Sun & Liu 2024a), it is still unclear why these stars undergo intense outbursts, creating the dense CSM, shortly before explosion. SESNe could originate from single massive Wolf–Rayet (WR) stars (Woosley & Weaver 1986), stripped by wind, or from binary systems, where the progenitor is stripped by a companion star (Podsiadlowski, Joss & Hsu 1992; Maeda et al. 2006, 2014, 2015; Crockett et al. 2008; Folatelli et al. 2015; Lyman et al. 2016; Fang & Maeda 2018; Taddia et al. 2018; Woosley, Sukhbold & Kasen 2021; Niu, Sun & Liu 2024b; Zhao et al. 2025). It still remains an open question what fraction of SESNe each channel contributes to.

For massive stars, stellar mass is the most important parameter that determines their structure and evolution. In addition, metallicity also plays a crucial role; at high metallicities, stars have stronger line-driven winds, allowing for the stripping of the envelope and the formation of CSM (Castor, Abbott & Klein 1975). These effects can determine the light curve and spectral features, and even the classification, of their final SN explosion. Environmental studies offer a powerful approach to investigate the metallicity of CCSNe. During the short lifetimes ($\lesssim 50\,\mathrm{Myr}$) of massive stars, they can travel only a short distance from the formation to explosion sites and the environment has limited chemical evolution over such short time-scales (Anderson et al. 2015).

Early studies on SN metallicity relied on long-slit spectroscopy (Anderson et al. 2010; Leloudas et al. 2011; Modjaz et al. 2011; Sanders et al. 2012; Taddia et al. 2015) or even used the metallicity of the entire host galaxy as a proxy (Langer & Norman 2006; Prieto, Stanek & Beacom 2008; Neill et al. 2011; Lunnan et al. 2014). It has been suggested, however, that a high spatial resolution is necessary for the accurate measurement of SN metallicity based on gas emission lines from the environment (Niino, Nagamine & Zhang 2015). In more recent years, integral-field-unit (IFU) spectroscopy has been used to investigate SN metallicity (Kuncarayakti et al. 2012a, 2013a, b, 2015, 2018; Galbany, Stanishev & Mourão 2014; Galbany et al. 2016, 2018; Moriya et al. 2023; Pessi et al. 2023). Instead of a single point or slit, IFU spectroscopy has the capability of acquiring spatially resolved spectral information over relatively large fields of view. This is important to reveal the complexity of the SN environment. A generally increasing trend in metallicity has been suggested for IIP → IIb → Ib → Ic, correlated with the degree of envelope stripping.

Within the domain of statistical research, minimizing sample bias is of particular importance. Limited by the telescopes' small field of view, early SN searches targeted galaxies of high masses and star formation rates (SFRs) in order to maximize the number of discovered SNe. Such galaxies, however, also tend to have higher metallicities (Tremonti et al. 2004), thus introducing a bias to SN samples discovered in this way (Sanders et al. 2012). With the increasing power of time-domain observations, more recent wide-field SN searches are able to map a significant portion of sky, for example, the All-Sky Automated Survey for SNe (ASAS-SN; Kochanek et al. 2017). SNe discovered by such untargeted searches are not affected by the metallicity bias introduced by their host galaxies. Fig. 1 compares the host galaxy magnitudes of CCSNe discovered before 2010, when most were discovered by targeted searches, and after 2016, when most were discovered by untargeted searches. The SNe in these statistics are sourced from the Transient
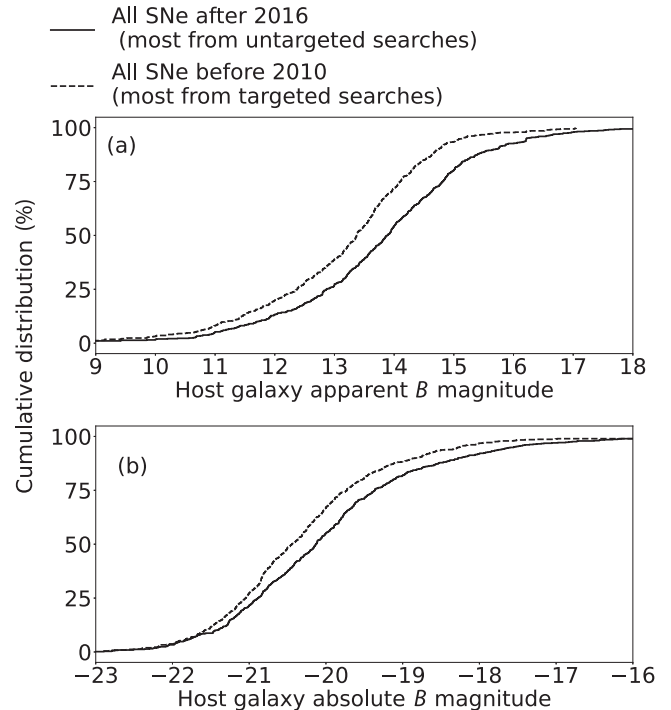
Figure 1. Cumulative distributions of the (a) apparent and (b) absolute *B*-band magnitudes of SN host galaxies. The dashed line is for SNe before 2010, when most were discovered by transient surveys targeted towards bright galaxies, while the solid line is for those after 2016, when most were discovered by untargeted SN searches.

Name Server[1] (TNS) and the Open SN Catalog (OSC; Guillochon et al. 2017), with an additional selection criterion of redshift less than 0.05. At such proximities, the searches for SNe with typical luminosities are very complete. Magnitudes for SN host galaxies are from the GLADE+ catalogue (Dálya et al. 2018). Some of the SNe lack this information for their host galaxies, and we have excluded these from the analysis. It is clear that SNe from targeted searches are significantly biased toward brighter host galaxies. Therefore, the early studies on SN metallicity are unavoidably affected by the bias caused by targeted SN discovery.

For studies that rely on archival observations, another potential bias may come from data availability as the archival observations are from different programmes with different scientific goals, target selection criteria, observational strategies, and even telescopes. Without further careful selection, the sample could be heterogeneous with significant biases that are difficult to assess.

A large sample size is also very important to reduce the stochastic sampling effect. In this work, we study SN metallicity based on IFU observations carried out by the Multi-Unit Spectroscopic Explorer (MUSE) on the Very Large Telescope (VLT). With a careful selection, we build a large and untargeted sample of 161 CCSNe, which is to date the largest SN sample with IFU data. We try to look for metallicity differences among the SN types. Our aim is to explore the possible roles played by metallicity in the origin of CCSNe.

This paper is organized as follows. In Section 2, we explain our sample selection and metallicity measurement. In Section 3, we present our results along with a discussion of key implications. Finally, we summarize our work in Section 4.

2 METHOD

2.1 Sample selection

The MUSE is an IFU instrument installed on the VLT operated by the European Southern Observatory (ESO) in Chile. It has a large field of view of 1×1 arcmin^2 and covers a wavelength range from 4650 to 9300 Å (Bacon et al. 2010). This range covers the important gas emission lines (such as Hα, Hβ, [O III] $\lambda\lambda$4959, 5007, and [N II] $\lambda\lambda$6548, 6583), with which metallicity can be derived using the strong-line method (Pagel et al. 1979; Edmunds & Pagel 1984). The MUSE is therefore very suitable for SN metallicity studies.

As mentioned in the introduction, further careful selection is crucial to construct a minimally biased sample for the statistical analysis of SN metallicities. The two key considerations are SN discovery and data availability.

2.1.1 SN discovery

As mentioned in the introduction, it is very important to avoid the bias by targeted SN searches. Therefore, we include in our sample only SNe discovered by the untargeted, wide-field transient surveys. Such surveys include the (Intermediate) Palomar Transient Factory (PTF; Law et al. 2009; Cao, Nugent & Kasliwal 2016), ZTF (Bellm et al. 2019), ASAS-SN (Kochanek et al. 2017), Pan-STARRS (Chambers et al. 2019), the Asteroid Terrestrial-impact Last Alert System (ATLAS; Jedicke et al. 2012), the Mobile Astronomical Systems of the Telescope-Robots (MASTER; Lipunov 2003), Gaia (Altavilla et al. 2012), the Catalina Sky Survey (CSS; Christensen 2014), the Sloan Digital Sky Survey (SDSS; Frieman et al. 2008) and the La Silla-QUEST Variability Survey (LSQ; Hadjiyska et al. 2012). In addition, we require the redshift to be $z < 0.05$, within which the giant H II regions of hundreds of parsec can be spatially resolved. We cross-match these SNe, queried from the TNS and OSC, with the ESO Data Archive,[2] obtaining 260 SNe with MUSE data.

2.1.2 Data availability

Given the wide field of view of the MUSE IFU spectrograph, distant and low-mass galaxies with small angular diameters are less likely to be observed. Fig. 2 shows the host magnitude distribution for the above-selected SNe with MUSE data at different redshifts. For comparison, we use all SNe discovered after 2016 as a reference. It is clear that SNe with $0.02 < z < 0.05$ are systematically biased toward brighter host galaxies. However, SNe with $z \leq 0.02$ are similar to the reference sample. Therefore, we further apply a redshift cut of $z \leq 0.02$. Note that the MUSE data were compiled from different observing programmes with different original scientific goals and target selection strategies. It is difficult to analyse the possible bias introduced by this heterogeneity. As shown in Fig. 2, however, the sample at $z \leq 0.02$ is quite representative of the local SN population and we deem the possible bias could be small. It is also worth noting that, although each transient survey has its own limiting magnitude, cadence and filter set, the CCSN subtypes considered in our sample, that is, Type II(P), IIb, Ib and Ic, exhibit very similar peak magnitudes and characteristic light-curve time-scales of the order of months. By restricting our sample to $z \leq 0.02$, we are confident that the discovery of local CCSNe by the current wide-field surveys is complete out to this redshift.
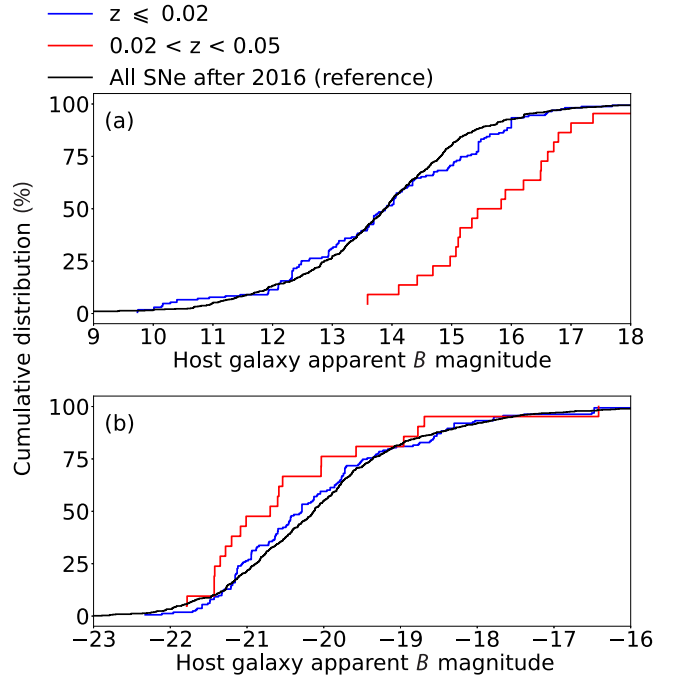
Figure 2. Cumulative distributions of the (a) apparent and (b) absolute *B*-band magnitudes of SN host galaxies. The black line is for all SNe after 2016, when most were discovered by untargeted SN searches (the same as the black solid line in Fig. 1). They suffer little from discovery bias and are used as a reference distribution. The blue and red lines are SNe discovered by untargeted searches and with MUSE observations at redshifts of $z \leq 0.02$ and $0.02 < z < 0.05$, respectively.

After the above selection, there are 24 SNe of Type IIP, 7 of Type IIn, 14 of Type IIb, 20 SNe of Type Ib, and 14 of Type Ic. In addition, there are 86 Type II SNe in our sample, for which the subtypes are unknown. Given that the overwhelming majority of Type II SNe are standard Type IIP SNe, we combined all SNe of Type IIP and Type II into a single subsample for analysis. We hereafter designate this subsample as Type II(P). Moreover, there are also two peculiar Type II, three peculiar Type Ib, one peculiar Type Ic, one Type Ibn, one Ca-rich Type Ib/Ic, five broad-lined Type Ic (Ic-BL), one Type Ib/c-BL, and three ambiguous Type IIn/LBV; these peculiar or ambiguous SNe are not included in our analysis, leaving 166 SNe in the sample. In the subsequent analysis, 5 SNe were found to lack reliable metallicity estimates and were excluded, leaving a final sample of 161 events. Details of the final sample are provided in Table A1, and the distribution of SN types is shown in Fig. 3.

2.2 Metallicity measurement

The reduced MUSE datacube was obtained from the ESO Data Archive. We used the IFUANAL package (Lyman et al. 2018) to analyse the datacube. First, we dereddened the datacube with Galactic extinction from Schlafly & Finkbeiner (2011), and a standard extinction law with $R_V = 3.1$ (Cardelli, Clayton & Mathis 1989). We then applied redshift corrections to the datacube with redshifts from OSC and TNS. To acquire the spatially resolved metallicity distribution across the galaxies, we employed the Voronoi binning with a target signal-to-noise ratio (S/N) of 120 within the wavelength range of 6540–6580 Å, within which the Hα + [N II] lines reside. As described later, a minimum of 10 bins is required to fit the metallicity gradients; if
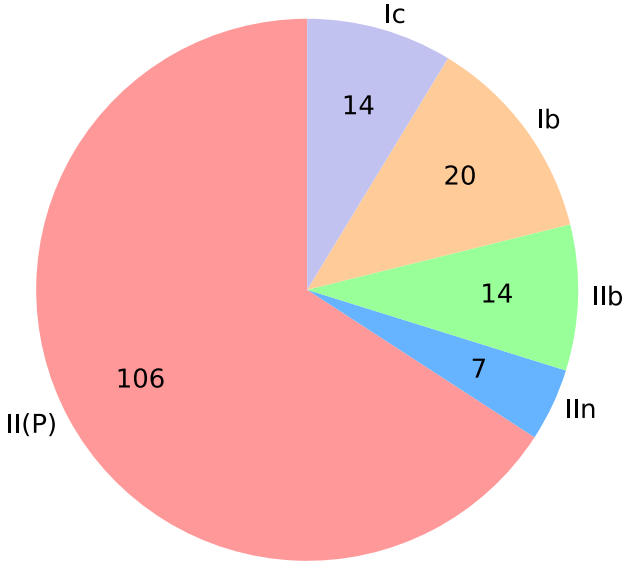
Figure 3. Number of SNe of different types in the final sample.

Figure 4. Comparison of SN metallicities obtained via the gradient method and directly from the local environment. The error bars indicate the typical uncertainties: 0.18 for the local environment method and 0.10 (median) for the gradient method.

fewer than 10 bins were found, we reduced the target S/N until 10 bins were achieved from the Voronoi binning. Due to differences in observation conditions and intrinsic galaxy properties, the number of bins for each galaxy varied from tens to several hundreds.

Inside each bin, we used STARLIGHT (Cid Fernandes et al. 2005) to fit and remove the stellar continuum, leaving only the nebular emission lines from ionized gas. Gaussian fitting is used to derive the fluxes of lines including Hα, Hβ, [O III]$\lambda\lambda$4959, 5007, and [N II]$\lambda\lambda$6548, 6583. We determined the gas-phase metallicity using the strong-line method based on the O3N2 calibration from Marino et al. (2013), a method that uses the ratio of strong lines with similar wavelengths, making it insensitive to extinction:

$$12 + \log(\mathrm{O/H}) = 8.533 - 0.214 \times \mathrm{O3N2}, \qquad (1)$$

where

$$\mathrm{O3N2} = \log \left(\frac{[\mathrm{O\,III}]\lambda 5007}{\mathrm{H}\beta} \times \frac{\mathrm{H}\alpha}{[\mathrm{N\,II}]\lambda 6583} \right). \qquad (2)$$

For bins where [O III] or Hβ were not detected (i.e. with amplitudes less than three times the spectral noise fluctuations), we used the N2 calibration instead:

$$12 + \log(\mathrm{O/H}) = 8.743 + 0.462 \times \mathrm{N2}, \qquad (3)$$

where

$$\mathrm{N2} = \log \left(\frac{[\mathrm{N\,II}]\lambda 6583}{\mathrm{H}\alpha} \right). \qquad (4)$$

If the [N II] emission line was also too weak to be reliably detected, we tried to estimate an upper limit for the metallicity. Specifically, we derived the [N II] linewidth using the observed Hα linewidth and the wavelength-dependent line spread function model of MUSE (Guérou et al. 2017). This width, combined with the 3σ amplitude limit, allowed us to estimate an upper limit of the [N II] line flux and, in turn, an upper limit of the metallicity.

The typical measurement uncertainty is 0.18 dex for the strong-line method (Marino et al. 2013). To reduce the metallicity uncertainties for the SNe, we used the galaxy metallicity gradient, calculated based on a large number of bins, to constrain the metallicity at the SN position. By using the spatial distribution characteristics of
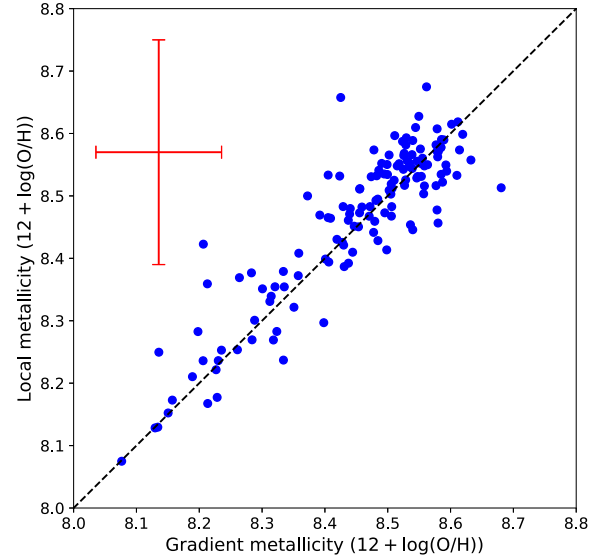
galaxy-wide metallicity, gradient fitting integrates information from multiple observation points, reduces the impact of local measurement uncertainties and enables safe extrapolation within a certain range. This effectively reduces the uncertainty in estimating metallicity at the SN position. Furthermore, some observations are made after the SN explosion, where the local spectra are contaminated by the SN's light. The method of estimating the metallicity at the explosion site using metallicity gradients can effectively mitigate this contamination.

To calculate the metallicity gradient, we first removed the bins that do not correspond to star-forming regions using the Baldwin–Phillips–Terlevich (BPT) diagram (Baldwin, Phillips & Terlevich 1981), adopting the maximum starburst line of Kewley et al. (2001). Then, for each Voronoi bin, we calculated the deprojected distances to the galaxy centre using the inclination and position angles from HyperLEDA; for some host galaxies, this information is not available and we derived the inclination and position angles by manually fitting the images. We fit the metallicity gradient using Bayesian regression, assuming Gaussian uncertainties for the individual metallicity measurements. The derived gradient was then used to estimate the metallicity at the SN position. In some circumstances, the SNe reside outside of, but not too far away from, the distance range, so we could safely extrapolate the gradient to derive the metallicity.

For some galaxies, it is difficult to fit a metallicity gradient, including the edge-on galaxies, for which we could not derive the deprojected distances, and those galaxies with too few Voronoi bins. In such cases, we calculated the metallicity from a local bin centred on the SN with a radius of 300 pc or the seeing-limited spatial resolution, whichever is larger. For SN2016hbb, SN2018eog and SN2018dfh, we had to use a local bin to measure their metallicity, but the SNe were still very bright during the observations; therefore, we could not obtain an accurate metallicity measurement because of the SN contamination. These three were excluded from our analysis.

Fig. 4 compares the metallicity determined via the gradient method and those obtained directly through local environment. The two sets of measurements are consistent within uncertainties. However, the metallicity uncertainty derived via the gradient method (with a
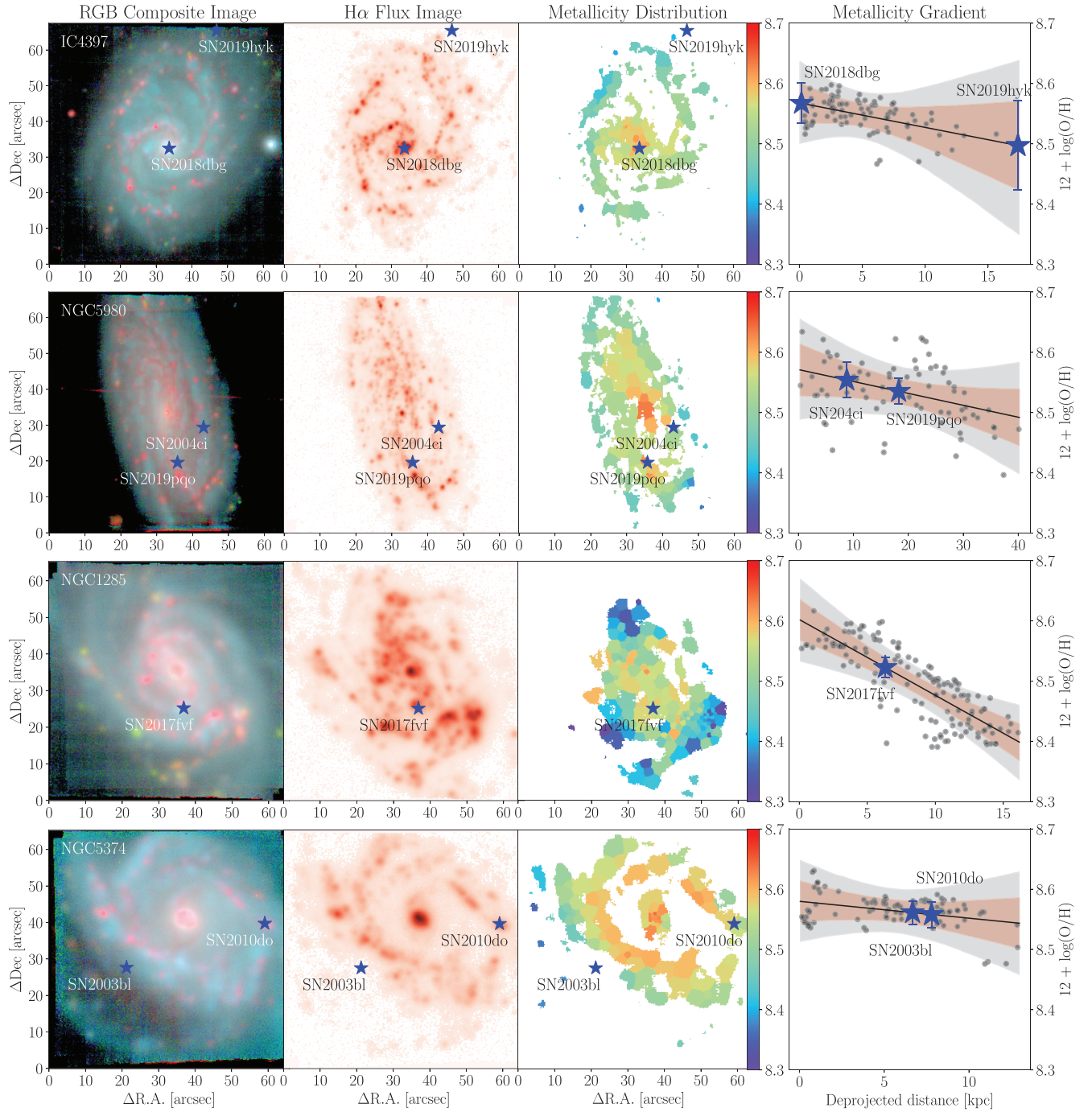
Figure 5. Example results of metallicity measurements for seven SNe located in four host galaxies. Column 1 shows RGB images of host galaxies generated from the MUSE datacube. The RGB components correspond to the cumulative fluxes from three spectral bands: 6550–6750, 4950–5150 and 4750–4950 Å, respectively. Column 2 shows Hα flux maps generated by simulating narrow-band filter (6548–6578 Å) observations of the MUSE datacube. The continuum is fitted and subtracted using flux measurements from two adjacent wavelength bands: 6488–6518 Å on the blue side and 6608–6638 Å on the red side of the emission line. The colour scale is in arbitrary units. Column 3 shows metallicity distribution maps derived with the strong-line method. Column 4 shows metallicity gradient fitting results. Black dots represent metallicity measurements for individual bins. The solid line shows the Bayesian regression fit for the metallicity gradient, while the red and grey shaded regions indicate the 1σ and 2σ confidence intervals, respectively. The blue stars mark the SN locations.

median value of 0.1 dex) is markedly smaller than that obtained directly from the local environment (0.18 dex). Moreover, the gradient approach effectively circumvents issues arising from explosion sites where the metallicity falls below the detection limit or is affected by contamination from SN light.

3 RESULTS AND DISCUSSION

With the method described above, we derived the metallicity for all SNe in our sample (listed in Table A1). For example, Fig. 5 displays the RGB composite images, H II regions, metallicity maps and metallicity gradients of four host galaxies, with which we derived the
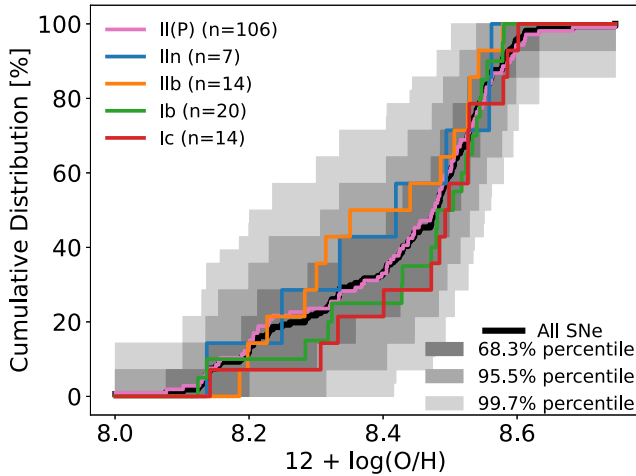
Figure 6. Cumulative metallicity distributions for different types of CCSNe. The black line represents the metallicity distribution for all SNe in the sample. The grey-shaded regions (from dark to light) indicate the 1σ, 2σ and 3σ uncertainties caused by the stochastic sampling effect for a subsample with $N = 14$, as estimated from our random resampling experiment.

Table 1. Mean, median and standard deviation values of $12 + \log(O/H)$ for different SN types. The errors originate from measurement uncertainties.

| SN Type	Number	Mean (dex)	Median (dex)	Standard deviation (dex)
II(P)	106	8.42 ± 0.01	8.47 ± 0.01	0.19
IIn	7	8.39 ± 0.05	8.42 ± 0.05	0.20
IIb	14	8.39 ± 0.03	8.40 ± 0.04	0.18
Ib	20	8.44 ± 0.02	8.48 ± 0.02	0.17
Ic	14	8.46 ± 0.03	8.51 ± 0.03	0.17

metallicities for seven SNe. Fig. 6 shows the cumulative metallicity distributions for all SNe and for different types. For SN2014cw and SN2016dsb, the [N II] lines are below the detection limit, allowing only upper limits to be determined; therefore, they are not included in Fig. 6. The metallicities span the range $12 + \log(O/H) = 8.1$–8.7 dex. Assuming Gaussian measurement errors, we employed a multiple resampling approach to calculate the mean, median and standard deviation values of the metallicity distributions (the results are listed in Table 1). The mean and median values are typically 8.4–8.5 dex, and the standard deviations are typically 0.17–0.20 dex. The differences among different SN types are very small. Type IIb and Type Ic have apparently the most different metallicity distributions, with mean (median) values of 8.39 (8.40) and 8.46 (8.51), respectively.

3.1 Is there any significant metallicity difference among SN types?

For the derived metallicity distributions, we carried out an experiment to study whether the apparent difference among SN types is real or due to the stochastic sampling effect. We used the metallicity distribution of all SNe, regardless of types, as a reference distribution. We then randomly drew $N = 14$ SNe (i.e. the number of SNe for Types IIb and Ic in our sample) from the full sample and plotted their metallicity distribution. This process was repeated 10 000 times to show how the metallicity distributions vary due to the stochastic sampling effect. The results are shown in Fig. 6. The stochastic sampling effect can cause a 1σ uncertainty of ~0.05 dex
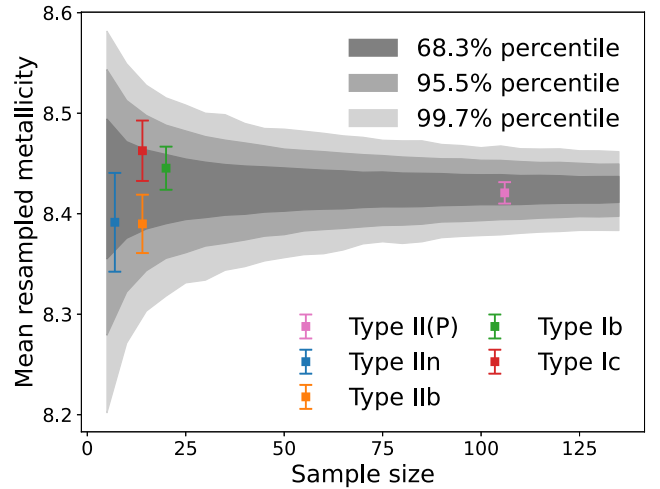
Figure 7. Data points: the number and mean metallicities for different types of CCSNe. The error bars are propagated from individual metallicity measurement uncertainties. Shaded regions show the 1σ, 2σ and 3σ (from dark to light) distributions of the mean values of randomly resampled SN metallicities from the full sample.

in the distributions. The metallicity distributions for different SN types are all consistent with the reference distribution within $\sim 1\sigma$ uncertainties.

We also performed the above experiment by varying the number of randomly chosen SNe. Fig. 7 shows the probability distributions of the mean values of the resampled SN metallicities as a function of sample size. For the Types II(P), IIn, IIb, Ib and Ic, the typical uncertainty for their mean metallicities caused by stochastic sampling is ~0.05 dex, much larger than those propagated from metallicity measurement errors (Table 1). The measured mean metallicities for different SN types are all consistent with that of the reference distribution within 1σ uncertainties. Therefore, the metallicity distributions of different SN types are not significantly different and are all consistent with being randomly drawn from the same reference distribution.

As an alternative method, we carried out a Kolmogorov–Smirnov (KS) test and calculated a p-value for each pair of SN types. In the KS test, the p-value assesses the degree of agreement between two sample distributions. Typically, a p-value less than 0.05 indicates a statistically significant difference between the two samples; conversely, a p-value greater than 0.05 indicates insufficient evidence to reject the null hypothesis that the two samples are drawn from the same distribution. The results are shown in Fig. 8. The p-values are generally very large, suggesting very weak metallicity differences among SN types. Even for the apparently most distinct Type IIb and Type Ic, the p-value is ~0.4 and not small enough to indicate a significant metallicity difference between the two types. In addition, Type II(P) SNe do not exhibit significant differences compared the the SESNe (IIb+Ib + Ic) grouped together.

3.2 Comparison with previous results

Sanders et al. (2012) studied the environments of a sample of SNe discovered by untargeted SN searches. They observed 75 Types IIb, Ib, Ic and Ic-BL SNe using the 6.5-m Magellan Telescopes at Las Campanas Observatory in Chile. They claimed a marginally significant difference between Type Ib and Type Ic SNe (with a p-value of ~0.1 from the KS test) and suggested that this difference

KS Matrix for Metallicity

KS Matrix for Metallicity

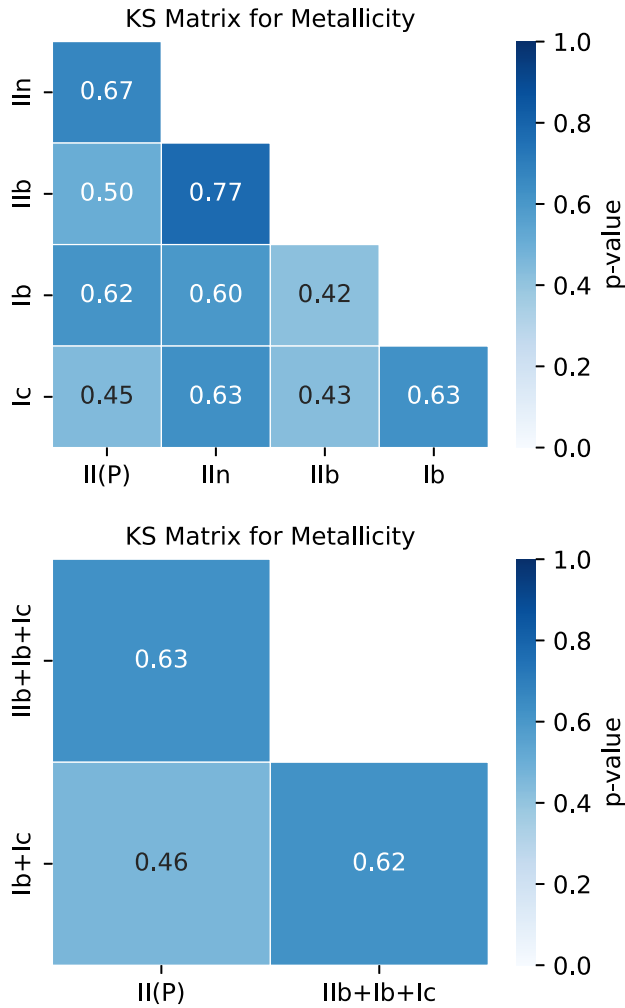**Figure 8.** The *p*-value from the KS test for each pair of SN types.

may influence $\lesssim 30$ per cent of stellar winds. This study relied on long-slit spectroscopy, however, and was unable to spatially resolve the host galaxies.

Kuncarayakti et al. (2012a, b, 2013a, b, 2015, 2018) pioneered the use of IFU spectroscopy to study SN environments. They investigated ~100 SNe of different types based on observations with VLT (MUSE, VIMOS and SINFONI), Gemini-North (GMOS) and the Hawaii 2.2-m telescope (SNIFS). They found no significant metallicity differences among SN types (Kuncarayakti et al. 2018). By the time of their studies, however, most SNe were discovered by targeted searches and it is unclear whether this potential bias may influence their sample.

Galbany et al. (2016, 2018) compiled a large collection of SN host galaxies (i.e. the PISCO sample) based on IFU observations with the 3.5-m CAHA telescope at the Calar Alto Observatory in Spain. Their sample contained 272 SNe (including 120 Type Ia SNe and 152 CCSNe) in 232 host galaxies. As noticed by themselves, most SNe in their sample were from targeted searches, therefore introducing a bias in the derived metallicity distributions. They also constructed a minimally biased sample from archival data and found that Type II(P) and Type Ic SNe display the highest metallicities while Type IIb and Type Ib SNe have lower metallicities. However, their KS test shows that this difference is not very significant.

Pessi et al. (2023) conducted IFU observations with the VLT/MUSE of a minimally biased sample of CCSNe discovered by the ASAS-SN survey (i.e. the AMUSING programme). Their sample included a total of 112 CCSNe and they did not find any significant metallicity differences among the SN types. However, most SNe in their sample are of Type II and very few are of the other types (9 IIn, 7 IIb, 7 Ib, 4 Ic, 3 Ibn, 2 Ic-BL), so their result may suffer more from the stochastic sampling effect.

In summary, the previous studies have not found any significant metallicity differences among the main CCSN types, II(P), IIn, IIb, Ib and Ic. Now, based on a larger and minimally biased sample with IFU observations, our study further confirms this conclusion. The typical uncertainty caused by stochastic sampling is narrowed down to ~0.05 dex and our careful analysis shows that all the SN types are consistent within a $\sim 1\sigma$ level.

3.3 The role of metallicity in SN progenitors

In the single-star progenitor channel, SESNe originate from massive WR stars, whose outer envelopes are stripped by their stellar winds (Conti 1978). The strength of line-driven wind is very sensitive to metallicity (Castor et al. 1975; Kudritzki & Puls 2000; Vink, de Koter & Lamers 2001) and one may expect an increasing trend in metallicity for Types IIP, IIb, Ib and Ic with increasing degrees of envelope stripping. However, our result shows no significant metallicity difference between these SN types. It is possible that the binary progenitor channel dominates the origin of most SESNe. In this case, the dependence on metallicity is minimal, while binary parameters (such as orbital separation and secondary-to-primary mass ratio) exert a greater influence. This conclusion is consistent with those based on the SN fraction (Smith et al. 2011), direct progenitor/companion detections (Crockett et al. 2008; Folatelli et al. 2015; Sun, Maund & Crowther 2020; Niu et al. 2024b), nebular spectroscopy (Maeda et al. 2006, 2014, 2015; Fang & Maeda 2018) and light-curve modelling (Lyman et al. 2016; Taddia et al. 2018; Woosley et al. 2021).

Although not as sensitive as stellar wind, the stripping of envelopes via binary interaction is not independent of metallicity. Recent studies suggest that Roche lobe stripping may become significantly less efficient at low metallicities (Götberg, de Mink & Groh 2017). In high-metallicity stars, the greater opacity in the outer layers can trap radiation and the higher radiative pressure can help to expel the hydrogen envelope. In low-metallicity stars, however, the lower opacity allows radiation to escape more easily, thus reducing the radiative pressure and keeping the hydrogen envelope cooler and more tightly bound. Therefore, it is easier for a low-metallicity mass donor to retain a significant hydrogen envelope after binary interaction, and this will result in a Type IIb, instead of a Type Ib, SN explosion. In our result, Type IIb SNe seem to have the lowest metallicities, but this difference is not significant enough to support this hypothesis. Future studies with even larger samples will be necessary to reveal the possible metallicity differences among SN types.

4 SUMMARY AND CONCLUSIONS

In this work, we have studied the metallicity of CCSNe based on a large and minimally biased sample with IFU observations. We carefully selected nearby CCSNe with archival VLT/MUSE data by considering the potential biases introduced by SN discovery and data availability. The final sample contains 161 CCSNe at a redshift of $z \leq 0.02$ discovered by untargeted SN searches, covering the main CCSN

types of II(P), IIn, IIb, Ib and Ic. Such a sample is representative of the SN population in the local Universe and is, to date, the largest sample for SN metallicity studies based on IFU observations.

For each SN host galaxy, we derived the spatially resolved metallicity map with the strong-line method and estimated the SN metallicity with the galaxy metallicity gradient. The derived metallicities are in the range $12 + \log(O/H) = 8.1–8.7$ dex; for different SN types, the mean and median values are typically 8.4–8.5 dex, and the standard deviations are typically 0.17–0.20 dex.

With a random resampling experiment and a KS test, we show that there is no significant metallicity difference among the analysed SN types. They can all be considered as being drawn randomly from the same reference distribution. With our large sample, the uncertainty caused by the stochastic sampling effect is narrowed down to ~ 0.05 dex, and the metallicity distributions of different SN types are all consistent within $\sim 1\sigma$ uncertainties.

In the single-star progenitor channel, where mass loss is dominated by metallicity-dependent line-driven wind, we expect an increasing trend of metallicity for IIP $\rightarrow$ IIb $\rightarrow$ Ib $\rightarrow$ Ic with increasing degrees of envelope stripping. However, our result suggests that metallicity plays a very minor role in the origin of SESNe. It is possible that most SESNe are from the binary progenitor channel, where the final fate of massive stars is insensitive to metallicity but is primarily determined by the binary parameters (e.g. secondary-to-primary mass ratio, binary separation).

Some theoretical studies suggest that Robe lobe stripping becomes less efficient at low metallicities such that the progenitor may retain a significant hydrogen envelope and result in a Type IIb SN explosion. In our results, although the metallicities of Type IIb SNe are lower by more than 1σ uncertainties, they are still consistent with the reference distribution within 2σ uncertainties. Future studies with even larger samples will be necessary to reveal the possible metallicity differences among SN types.

DATA AVAILABILITY

Based on observations collected at the European Southern Observatory under ESO programme(s): 60.A-9319(A), 097.B-0640(A), 106.210Z.008, 096.B-0309(A), 106.210Z.009, 098.B-0193(A), 110.23ZH.001, 097.B-0518(A), 111.24VQ.001, 60.A-9301(A), 095.B-0686(A), 1100.B-0651(B), 0101.D-0748(A), 095.D-0172(A), 0104.D-0503(A), 104.20VC.001, 0103.D-0440(A), 0103.A-0637(A), 096.D-0263(A), 106.2155.001, 0101.B-0368(B), 1100.B-0651(A), 096.D-0296(A), 1100.B-0651(D), 0104.B-0404(A), 097.B-0165(A), 108.229J.001, 095.B-0042(A), 097.B-0041(A), 0100.D-0341(A), 094.B-0733(B), 108.21ZY.008, 0101.A-0282(A), 099.A-0870(A), 106.2104.001, 0102.B-0794(A), 111.24UM.001, 0101.B-0706(A), 110.24AS.002, 0100.B-0116(A), 097.D-0408(A), 099.B-0242(A), 099.D-0022(A), 108.229G.001, 094.B-0298(A)

REFERENCES

Altavilla G., Botticella M. T., Cappellaro E., Turatto M., 2012, Ap&SS, 341, 163
Anderson J. P., Covarrubias R. A., James P. A., Hamuy M., Habergham S. M., 2010, MNRAS, 407, 2660
Anderson J. P., James P. A., Habergham S. M., Galbany L., Kuncarayakti H., 2015, PASA, 32, e019
Arnett W. D., Bahcall J. N., Kirshner R. P., Woosley S. E., 1989, ARA&A, 27, 629
Bacon R. et al., 2010, Proc. SPIE, 7735, 773508
Baldwin J. A., Phillips M. M., Terlevich R., 1981, PASP, 93, 5
Barbon R., Ciatti F., Rosino L., 1979, A&A, 72, 287
Beasor E. R., Smith N., Jencson J. E., 2025, ApJ, 979, 117
Bellm E. C. et al., 2019, PASP, 131, 018002
Bethe H. A., Brown G. E., Applegate J., Lattimer J. M., 1979, Nucl. Phys. A, 324, 487
Bostroem K. A. et al., 2023, ApJ, 953, L18
Cao Y., Nugent P. E., Kasliwal M. M., 2016, PASP, 128, 114502
Cardelli J. A., Clayton G. C., Mathis J. S., 1989, ApJ, 345, 245
Castor J. I., Abbott D. C., Klein R. I., 1975, ApJ, 195, 157
Chambers K. C. et al., 2019, The Pan-STARRS1 Surveys, preprint (arXiv:1612.05560)
Christensen E., 2014, in Wozniak P. R., Graham M. J., Mahabal A. A., Seaman R., eds, The Third Hot-wiring the Transient Universe Workshop. Los Alamos National Laboratory, Los Alamos, NM, p. 55
Cid Fernandes R., Mateus A., Sodré L., Stasińska G., Gomes J. M., 2005, MNRAS, 358, 363
Conti P. S., 1978, ARA&A, 16, 371
Crockett R. M. et al., 2008, MNRAS, 391, L5
Dálya G. et al., 2018, MNRAS, 479, 2374
Edmunds M. G., Pagel B. E. J., 1984, MNRAS, 211, 507
Elias-Rosa N. et al., 2016, MNRAS, 463, 3894
Fang Q., Maeda K., 2018, ApJ, 864, 47
Filippenko A. V., 1997, ARA&A, 35, 309
Folatelli G., Bersten M. C., Kuncarayakti H., Benvenuto O. G., Maeda K., Nomoto K., 2015, ApJ, 811, 147
Frieman J. A. et al., 2008, AJ, 135, 338
Gal-Yam A. et al., 2007, ApJ, 656, 372
Galbany L., Stanishev V., Mourão A., 2014, in Ray A., McCray R. A., eds, Proc. IAU Symp. Vol. 296, Supernova Environmental Impacts. Kluwer, Dordecht, p. 350
Galbany L. et al., 2016, A&A, 591, A48
Galbany L. et al., 2018, ApJ, 855, 107
Götberg Y., de Mink S. E., Groh J. H., 2017, A&A, 608, A11
Guérou A. et al., 2017, A&A, 608, A5
Guillochon J., Parrent J., Kelley L. Z., Margutti R., 2017, ApJ, 835, 64
Hadjiyska E. et al., 2012, in Griffin E., Hanisch R., Seaman R., eds, Proc. IAU Symp. Vol 285, New Horizons in Time Domain Astronomy. Kluwer, Dordrecht, p. 324(arXiv:1210.1584)
Jedicke R., Tonry J., Veres P., Farnocchia D., Spoto F., Rest A., Wainscoat R. J., Lee E., 2012, AAS/Division for Planetary Sciences Meeting Abstracts, 44, 210.12
Kewley L. J., Dopita M. A., Sutherland R. S., Heisler C. A., Trevena J., 2001, ApJ, 556, 121
Kiewe M. et al., 2012, ApJ, 744, 10
Kochanek C. S., 2014, ApJ, 785, 28
Kochanek C. S. et al., 2017, PASP, 129, 104502
Kudritzki R.-P., Puls J., 2000, ARA&A, 38, 613
Kuncarayakti H. et al., 2012a, in Roming P., Kawai N., Pian E., eds, Proc. IAU Symp. Vol. 279, Death of Massive Stars: Supernovae and Gamma-Ray Bursts. Kluwer, Dordrecht, p. 343
Kuncarayakti H. et al., 2012b, in Aoki W., Ishigaki M., Suda T., Tsujimoto T., Arimoto N., eds, ASP Conf. Ser. Vol. 458, Galactic Archaeology: Near-Field Cosmology and the Formation of the Milky Way. Astron. Soc. Pac., San Francisco, CA, p. 43
Kuncarayakti H. et al., 2013a, AJ, 146, 30
Kuncarayakti H. et al., 2013b, AJ, 146, 31

Kuncarayakti H. et al., 2015, Publication of Korean Astronomical Society, 30, 139

Kuncarayakti H. et al., 2018, A&A, 613, A35

Langer N., Norman C. A., 2006, ApJ, 638, L63

Law N. M. et al., 2009, PASP, 121, 1395

Leloudas G. et al., 2011, A&A, 530, A95

Lipunov V. M., 2003, American Astronomical Society Meeting Abstracts, 202, 47.02

Lunnan R. et al., 2014, ApJ, 787, 138

Lyman J. D., Bersier D., James P. A., Mazzali P. A., Eldridge J. J., Fraser M., Pian E., 2016, MNRAS, 457, 328

Lyman J. D. et al., 2018, MNRAS, 473, 1359

Maeda K., Nomoto K., Mazzali P. A., Deng J., 2006, ApJ, 640, 854

Maeda K., Katsuda S., Bamba A., Terada Y., Fukazawa Y., 2014, ApJ, 785, 95

Maeda K. et al., 2015, ApJ, 807, 35

Marino R. A. et al., 2013, A&A, 559, A114

Minkowski R., 1941, PASP, 53, 224

Modjaz M., Kewley L., Bloom J. S., Filippenko A. V., Perley D., Silverman J. M., 2011, ApJ, 731, L4

Moriya T. J. et al., 2023, A&A, 677, A20

Neill J. D. et al., 2011, ApJ, 727, 15

Niino Y., Nagamine K., Zhang B., 2015, MNRAS, 449, 2706

Niu Z., Sun N-C., Liu J., 2024a, ApJ, 966, L20

Niu Z., Sun N-C., Liu J., 2024b, ApJ, 970, L9

Nomoto K., Suzuki T., Shigeyama T., Kumagai S., Yamaoka H., Saio H., 1993, Nature, 364, 507

Pagel B. E. J., Edmunds M. G., Blackwell D. E., Chun M. S., Smith G., 1979, MNRAS, 189, 95

Pessi T. et al., 2023, A&A, 677, A28

Podsiadlowski P., Joss P. C., Hsu J. J. L., 1992, ApJ, 391, 246

Prieto J. L., Stanek K. Z., Beacom J. F., 2008, ApJ, 673, 999

Sanders N. E. et al., 2012, ApJ, 758, 132

Schlafly E. F., Finkbeiner D. P., 2011, ApJ, 737, 103

Schlegel E. M., 1990, MNRAS, 244, 269

Smartt S. J., 2009, ARA&A, 47, 63

Smith N., 2014, ARA&A, 52, 487

Smith N., Li W., Filippenko A. V., Chornock R., 2011, MNRAS, 412, 1522

Sun N.-C., Maund J. R., Crowther P. A., 2020, MNRAS, 497, 5118

Taddia F. et al., 2015, A&A, 580, A131

Taddia F. et al., 2018, A&A, 609, A136

Tremonti C. A. et al., 2004, ApJ, 613, 898

Vink J. S., de Koter A., Lamers H. J. G. L. M., 2001, A&A, 369, 574

Walmswell J. J., Eldridge J. J., 2012, MNRAS, 419, 2054

Woosley S. E., Weaver T. A., 1986, ARA&A, 24, 205

Woosley S. E., Sukhbold T., Kasen D. N., 2021, ApJ, 913, 145

Zapartas E., de Mink S. E., Justham S., Smith N., Renzo M., de Koter A., 2021, A&A, 645, A6

Zhao Y-H. et al., 2025, ApJ, 980, L6

APPENDIX: SN DATA WITH METALLICITY

Table A1. SN data with metallicity. PA denotes the position angle of the host galaxy, i is the inclination angle of the host galaxy and $12 + \log(\text{O/H})$ is the oxygen abundance at the SN location.

Name	Type	Host galaxy	Redshift	PA (deg)	i (deg)	$12 + \log(\text{O/H})$ grad. (dex)	$12 + \log(\text{O/H})$ local (dex)	Calibration
ASASSN-14dl	II	ESO 506-G4	0.0134	88.4	67.2	8.55(+0.05/−0.05)	8.53	O3N2
ASASSN-14dp	II	ESO 319-G15	0.0092	81.5	54.2	8.15(+0.09/−0.09)	−	O3N2
ASASSN-14dq	II	UGC 11860	0.0104	133.0	74.7	8.21(+0.08/−0.08)	8.42	O3N2
ASASSN-14ha	II	NGC 1566	0.0050	44.2	49.1	8.58(+0.02/−0.02)	8.52	O3N2
ASASSN-14ma	II	SDSS J235509.00+101252.9	0.0137	89.1	29.2	8.29(+0.04/−0.04)	8.30	O3N2
ASASSN-15bb	II	ESO 381-IG48	0.0159	110.6	59.1	8.14(+0.06/−0.06)	8.25	O3N2
ASASSN-15fi	II	MRK 884	0.0172	45.5	40.0	8.13(+0.01/−0.01)	8.13	O3N2
ASASSN-15fz	II	NGC 5227	0.0175	161.1	32.8	8.52(+0.06/−0.06)	8.54	O3N2
ASASSN-15jp	II	NGC 3157	0.0095	39.1	80.4	8.47(+0.05/−0.05)	−	O3N2
ASASSN-15ln	II	UGC 546	0.0150	3.3	77.8	8.21(+0.07/−0.07)	8.36	O3N2
ASASSN-15lx	II	ESO 47-G4	0.0126	90.5	48.7	8.21(+0.05/−0.05)	8.24	O3N2
ASASSN-15oz	II	HIPASS J1919-33	0.0069	−	−	−	8.66	O3N2
ASASSN-15qh	II	ESO 534-G024	0.0102	112.0	55.6	8.41(+0.09/−0.09)	−	O3N2
ASASSN-16ab	II	CGCG 012−116	0.0043	49.0	52.5	8.24(+0.05/−0.05)	8.25	O3N2
ASASSN-19kz	II	NGC 2207	0.0091	115.6	58.2	8.52(+0.03/−0.03)	−	O3N2
AT2018bbl	II	NGC 7421	0.0060	80.6	36.2	8.59(+0.07/−0.07)	8.54	O3N2
PS15aaa	II	IC 564	0.0190	68.2	77.3	8.51(+0.06/−0.06)	8.52	O3N2
PS15afa	II	NGC 3404	0.0150	81.3	86.7	8.60(+0.14/−0.14)	−	O3N2
PTF09gpn	II	Anonymous	0.0150	−	−	−	8.32	O3N2
SMT16atf	II	PGC098793	0.0140	110.0	0.0	8.41(+0.06/−0.06)	8.39	O3N2
SN1998dl	II	NGC 1084	0.0044	39.9	49.9	8.46(+0.01/−0.01)	8.51	O3N2
SN1999dh	II	IC 211	0.0110	56.0	64.7	8.40(+0.02/−0.02)	8.30	O3N2
SN2001J	II	UGC 4729	0.0130	85.0	35.2	8.36(+0.05/−0.05)	8.37	O3N2
SN2003E	II	ESO 485-G004	0.0149	142.9	90.0	−	8.31	O3N2
SN2003ao	II	NGC 2993	0.0081	93.7	35.8	8.44(+0.01/−0.01)	8.47	O3N2
SN2004F	II	NGC 1285	0.0175	8.1	59.3	8.51(+0.02/−0.02)	8.60	O3N2
SN2004ci	II	NGC 5980	0.0140	14.5	76.4	8.59(+0.03/−0.03)	8.52	O3N2
SN2005H	II	NGC 838	0.0128	77.2	49.8	8.53(+0.01/−0.01)	8.55	O3N2
SN2005Z	II	NGC 3363	0.0190	179.2	45.3	8.62(+0.06/−0.06)	8.60	O3N2
SN2006be	II	IC 4582	0.0071	172.1	83.1	8.37(+0.14/−0.14)	8.50	O3N2
SN2006ca	II	UGC 11214	0.0088	175.0	16.5	8.41(+0.06/−0.06)	8.46	O3N2
SN2006cx	II	NGC 7316	0.0185	66.0	32.9	8.52(+0.02/−0.02)	8.55	O3N2
SN2007rw	II	UGC 7798	0.0086	57.2	56.0	8.31(+0.06/−0.06)	8.33	O3N2
SN2008V	II	NGC 1591	0.0137	29.4	56.8	8.55(+0.04/−0.04)	8.53	O3N2

Table A1 – *continued*

Name	Type	Host galaxy	Redshift	PA (deg)	*i* (deg)	12 + log(O/H) grad. (dex)	12 + log(O/H) local (dex)	Calibration
SN2008aw	II	NGC 4939	0.0104	7.4	70.1	8.68(+0.19/−0.19)	8.51	O3N2
SN2008fq	II	NGC 6907	0.0106	57.7	37.5	8.58(+0.01/−0.01)	8.53	O3N2
SN2009H	II	NGC 1084	0.0047	39.9	49.9	8.46(+0.01/−0.01)	8.51	O3N2
SN2009K	II	NGC 1620	0.0117	22.9	81.2	8.61(+0.11/−0.11)	8.57	N2
SN2009au	II	ESO 443-G21	0.0094	159.6	79.0	8.46(+0.02/−0.02)	8.48	O3N2
SN2009dq	II	IC 2554	0.0046	4.1	70.8	8.58(+0.01/−0.01)	8.58	O3N2
SN2010F	II	NGC 3120	0.0093	6.2	47.5	8.51(+0.07/−0.07)	8.51	O3N2
SN2010K	II	A120246+0224	0.0200	–	–	–	8.13	O3N2
SN2010cl	II	MCG −02-25-20	0.0091	126.2	85.5	8.56(+0.11/−0.11)	–	O3N2
SN2012cc	II	NGC 4419	−0.0009	132.7	84.7	8.59(+0.06/−0.06)	–	O3N2
SN2012ga	II	NGC 6976	0.0200	164.9	27.1	8.50(+0.06/−0.06)	8.50	O3N2
SN2013ej	II	NGC 628	0.0022	25.0	19.8	8.51(+0.04/−0.04)	–	O3N2
SN2014V	II	NGC 3905	0.0193	62.5	48.7	8.53(+0.04/−0.04)	8.56	O3N2
SN2014cw	II	PGC 68414	0.0060	–	–	–	< 8.28	N2
SN2014ay	II	UGC 11037	0.0104	52.2	90.0	–	8.49	O3N2
SN2014cy	II	NGC 7742	0.0055	165.0	16.8	8.55(+0.01/−0.01)	8.53	O3N2
SN2014dw	II	NGC 3568	0.0082	7.0	67.0	8.48(+0.02/−0.02)	8.49	O3N2
SN2015ay	II	UGC 722	0.0140	136.9	90.0	–	8.20	O3N2
SN2016adl	II	GALEXASC J115155.68−132459.3	0.0070	–	–	–	8.07	O3N2
SN2016aqf	II	NGC 2101	0.0040	94.0	69.1	8.23(+0.06/−0.06)	8.18	O3N2
SN2016ase	II	ESO 504-G009	0.0150	123.1	47.0	8.14(+0.15/−0.16)	–	O3N2
SN2016bev	II	ESO 560-G013	0.0110	138.8	90.0	–	8.37	O3N2
SN2016blz	II	SDSS J154029.29+005437.4	0.0110	0.8	44.6	8.19(+0.06/−0.06)	8.21	O3N2
SN2016bsb	II	Anonymous	0.0200	–	–	–	8.17	O3N2
SN2016cyk	II	2MASX J13024397−2656276	0.0161	70.0	55.8	8.56(+0.04/−0.04)	8.55	O3N2
SN2016hgm	II	NGC 493	0.0080	59.9	74.6	8.44(+0.08/−0.08)	8.39	O3N2
SN2016hmq	II	PGC146262	0.0174	28.5	73.5	8.48(+0.07/−0.07)	8.44	O3N2
SN2016iyz	II	IC 2151	0.0104	93.4	61.5	8.49(+0.03/−0.03)	8.55	O3N2
SN2016zb	II	MCG −03-25-015	0.0140	120.2	18.6	8.19(+0.25/−0.25)	–	O3N2
SN2017ahn	II	NGC 3318	0.0090	79.4	59.8	8.50(+0.02/−0.02)	8.47	O3N2
SN2017ahn	II	NGC 3318	0.0090	79.4	59.8	8.46(+0.06/−0.06)	8.47	O3N2
SN2017auf	II	MCG −02-13-038	0.0133	111.3	73.6	8.61(+0.06/−0.06)	8.53	O3N2
SN2017faa	II	IC 4224	0.0180	99.3	84.2	8.39(+0.08/−0.08)	8.47	O3N2
SN2017fbq	II	2MASX J19334551−6058022	0.0150	161.0	81.1	8.33(+0.06/−0.06)	8.24	O3N2
SN2017fbu	II	IC 211	0.0109	56.0	64.7	8.40(+0.02/−0.02)	–	O3N2
SN2017ffq	II	2MASX J17401447−5825586	0.0127	140.8	74.4	8.45(+0.05/−0.05)	8.45	O3N2
SN2017fqk	II	NGC 1137	0.0150	16.1	59.5	8.48(+0.11/−0.11)	–	O3N2
SN2017fqo	II	NGC 716	0.0150	59.0	75.9	8.43(+0.19/−0.19)	8.42	O3N2
SN2017ggw	II	ESO-246-G-21	0.0180	140.7	52.4	8.51(+0.05/−0.05)	–	O3N2
SN2017gmr	II	NGC0988	0.0050	119.6	69.1	8.49(+0.03/−0.03)	–	O3N2
SN2017grn	II	IC 1498	0.0180	2.9	90.0	–	8.59	O3N2
SN2017hxv	II	ESO 466-G004	0.0160	134.4	41.3	8.60(+0.07/−0.07)	–	O3N2
SN2017jmk	II	NGC 7541	0.0095	101.6	74.8	8.48(+0.02/−0.02)	8.53	O3N2
SN2017pn	II	PGC 959170	0.0140	38.0	62.4	8.20(+0.07/−0.07)	–	O3N2
SN2018ant	II	MCG −02-22-22	0.0197	70.0	90.0	–	8.68	O3N2
SN2018bl	II	ESO 18-G9	0.0180	50.0	34.3	8.54(+0.06/−0.06)	8.45	O3N2
SN2018cuf	II	IC 5092	0.0108	26.9	28.6	8.61(+0.19/−0.19)	–	O3N2
SN2018cvn	II	ESO 476-G016	0.0190	141.1	59.6	8.45(+0.19/−0.20)	8.45	O3N2
SN2018dfg	II	NGC 5468	0.0095	109.2	21.1	8.56(+0.04/−0.04)	–	O3N2
SN2018evy	II	NGC 6627	0.0180	74.5	26.9	8.53(+0.03/−0.03)	8.55	O3N2
SN2018fit	II	CGCG 431−062	0.0140	130.6	81.5	8.54(+0.27/−0.27)	–	O3N2
SN2018hyw	II	UGC 4344	0.0168	89.4	27.7	8.42(+0.07/−0.08)	8.53	O3N2
SN2018ivc	II	NGC1068	0.0038	72.7	34.7	8.48(+0.00/−0.00)	8.43	O3N2
SN2018kcw	II	IC 5179	0.0120	60.6	62.2	8.55(+0.01/−0.01)	8.58	O3N2
SN2018lab	II	IC2163	0.0092	102.6	78.2	8.53(+0.01/−0.01)	8.56	O3N2
SN2018pq	II	IC 3896A	0.0060	105.0	48.4	8.53(+0.16/−0.15)	–	O3N2
SN2019dxd	II	NGC 3464	0.0125	110.8	50.8	8.54(+0.05/−0.05)	8.59	O3N2
SN2019hyk	II	IC 4397	0.0147	160.1	48.3	8.50(+0.07/−0.07)	–	O3N2
SN2019ltw	II	CGCG 137−076	0.0160	59.0	25.4	8.44(+0.05/−0.05)	8.46	O3N2
SN2019tua	II	UGC 11860	0.0104	133.0	74.7	8.16(+0.07/−0.06)	8.17	O3N2
SN2019xis	II	Anonymous	0.0050	–	–	–	8.15	O3N2
SN2020aqe	II	NGC 3836	0.0123	137.7	39.8	8.41(+0.02/−0.02)	8.47	O3N2
SN2020aze	II	NGC 3318	0.0090	79.4	59.8	8.55(+0.05/−0.05)	8.55	O3N2
SN2020jfo	II	M61	0.0050	162.0	18.1	8.58(+0.05/−0.05)	8.57	O3N2
SN2020llx	II	NGC 7140	0.0099	17.4	49.6	8.55(+0.08/−0.08)	8.55	O3N2

Table A1 – *continued*

Name	Type	Host galaxy	Redshift	PA (deg)	*i* (deg)	12 + log(O/H) grad. (dex)	12 + log(O/H) local (dex)	Calibration
SN2021abkm	II	NGC 6627	0.0176	74.5	26.9	8.58(+0.11/−0.11)	8.58	O3N2
SN2021agdm	II	ESO 61–8	0.0114	106.8	78.0	8.45(+0.12/−0.12)	–	O3N2
SN2021zgm	II	UGC 11289	0.0133	1.0	53.7	8.61(+0.18/−0.18)	–	O3N2
SN2022aau	II	NGC 1672	0.0044	154.9	28.9	8.55(+0.00/−0.00)	8.63	O3N2
SN2022acko	II	NGC 1300	0.0053	104.6	61.8	8.63(+0.10/−0.11)	8.56	O3N2
SN2022mmr	II	IC 1498	0.0173	2.9	90.0	–	8.59	N2
SN2022wsp	II	NGC 7448	0.0073	170.5	70.1	8.41(+0.01/−0.01)	8.53	O3N2
SN2023dpj	II	NGC 5135	0.0137	126.4	24.8	8.51(+0.02/−0.02)	8.47	O3N2
SN2023ijd	II	NGC 4568	0.0074	28.6	67.5	8.51(+0.02/−0.02)	–	O3N2
SN2023rve	II	NGC 1097	0.0040	133.9	54.8	8.75(+0.26/−0.25)	–	O3N2
SN2024jlf	II	NGC 5690	0.0058	145.1	75.9	8.47(+0.06/−0.06)	8.53	O3N2
ASASSN-14iz	IIP	ESO 462-G9	0.0193	162.3	58.8	8.48(+0.15/−0.15)	8.57	N2
ASASSN-15kz	IIP	IC 4303	0.0080	70.7	59.1	8.23(+0.04/−0.04)	8.24	O3N2
ASASSN-15ng	IIP	ESO 221-G12	0.0098	164.3	90.0	–	8.34	O3N2
ASASSN-16at	IIP	UGC 8041	0.0044	168.3	54.0	8.32(+0.07/−0.07)	8.35	O3N2
SN1999br	IIP	NGC 4900	0.0032	135.0	19.0	8.43(+0.02/−0.02)	8.39	O3N2
SN2003bl	IIP	NGC 5374	0.0146	45.0	36.9	8.54(+0.02/−0.02)	8.61	N2
SN2003bn	IIP	2MASX J10023529−2110531	0.0128	98.0	74.6	8.36(+0.06/−0.06)	8.41	O3N2
SN2003hg	IIP	NGC 7771	0.0143	68.0	66.7	8.58(+0.02/−0.02)	8.58	O3N2
SN2012bu	IIP	NGC 3449	0.0109	145.8	90.0	–	8.49	O3N2
SN2015W	IIP	UGC 3617	0.0130	8.5	49.0	8.10(+0.18/−0.18)	–	O3N2
SN2016B	IIP	CGCG 012–116	0.0043	49.0	52.5	8.26(+0.06/−0.06)	8.25	O3N2
SN2016I	IIP	UGC 09450	0.0149	49.0	90.0	–	8.12	N2
SN2016L	IIP	UGCA 397	0.0090	120.0	19.0	8.20(+0.05/−0.05)	–	O3N2
SN2016blb	IIP	2MASX J11372059−0454450	0.0180	168.0	67.5	8.33(+0.06/−0.06)	8.38	O3N2
SN2016cok	IIP	M66	0.0020	168.2	67.5	8.59(+0.03/−0.03)	8.59	O3N2
SN2016hvu	IIP	NGC 7316	0.0185	66.0	32.9	8.44(+0.02/−0.02)	8.41	O3N2
SN2017aym	IIP	NGC 5690	0.0058	145.1	75.9	8.51(+0.05/−0.05)	8.53	O3N2
SN2017ejx	IIP	NGC 2993	0.0081	93.7	35.8	8.47(+0.01/−0.01)	8.47	O3N2
SN2017fem	IIP	IC 4452	0.0140	77.8	20.6	8.50(+0.03/−0.03)	8.51	O3N2
SN2017fvf	IIP	NGC 1285	0.0170	8.1	59.3	8.50(+0.02/−0.02)	8.57	O3N2
SN2017fvr	IIP	UGC 3165	0.0130	135.0	61.0	8.42(+0.07/−0.07)	–	O3N2
SN2017gry	IIP	ESO 155-G36	0.0193	171.9	82.4	8.54(+0.05/−0.05)	8.54	O3N2
SN2017ivu	IIP	NGC 5962	0.0065	106.3	51.4	8.00(+0.18/−0.18)	–	O3N2
SN2018cho	IIP	IC 4	0.0167	12.0	45.6	8.56(+0.04/−0.04)	8.55	O3N2
SN2018yo	IIP	UGC 7840	0.0130	73.4	57.6	8.37(+0.09/−0.09)	–	O3N2
ASASSN-14fd	IIn	PGC 43070	0.0154	16.0	51.5	8.34(+0.07/−0.07)	8.35	O3N2
ASASSN-15hs	IIn	2MASX J15333488−7807258	0.0091	177.3	39.9	8.56(+0.03/−0.03)	8.52	O3N2
ASASSN-16jt	IIn	ESO 344-G021	0.0108	58.0	67.3	8.56(+0.06/−0.16)	8.67	O3N2
SN1997bs	IIn	NGC 3627	0.0019	168.2	67.5	8.59(+0.04/−0.04)	8.55	O3N2
SN2013fc	IIn	ESO 154-G10	0.0186	87.9	35.5	8.65(+0.05/−0.05)	–	O3N2
SN2015bf	IIn	NGC 7653	0.0142	172.5	31.0	8.49(+0.18/−0.18)	8.54	O3N2
SN2016aiy	IIn	ESO 323-G084	0.0100	7.0	77.7	8.25(+0.18/−0.18)	–	O3N2
SN2016eso	IIn	ESO 422-G019	0.0170	148.9	62.5	8.14(+0.32/−0.08)	–	O3N2
SN2021aefs	IIn	NGC 3836	0.0123	137.7	39.8	8.42(+0.01/−0.01)	8.43	O3N2
ASASSN-14az	IIb	PGC 1101367	0.0067	12.0	68.8	8.20(+0.13/−0.13)	8.28	O3N2
ASASSN-15bd	IIb	SDSS J155438.39+163637.6	0.0079	89.1	90.0	–	8.19	O3N2
ASASSN-15tu	IIb	2MASX J22340166−3223490	0.0126	65.0	38.6	8.35(+0.06/−0.06)	8.32	O3N2
PS15apj	IIb	NGC 6641	0.0140	100.0	29.9	8.51(+0.06/−0.06)	8.48	O3N2
SN2008aq	IIb	MCG −02-33-20	0.0080	175.0	90.0	–	8.14	O3N2
SN2014cl	IIb	IC 217	0.0063	35.1	82.6	8.27(+0.28/−0.28)	–	O3N2
SN2015bi	IIb	VV 839	0.0160	143.3	52.4	8.31(+0.08/−0.08)	8.34	O3N2
SN2016dsb	IIb	GALEXASC J015900.57−322225.2	0.0161	–	–	–	< 8.15	N2
SN2016gkg	IIb	NGC 613	0.0049	122.2	35.7	8.53(+0.18/−0.18)	8.59	N2
SN2016iyc	IIb	UGC 11924	0.0127	120.2	61.4	8.30(+0.05/−0.05)	8.35	O3N2
SN2017mw	IIb	ESO 316-G7	0.0120	158.7	70.0	8.23(+0.02/−0.02)	8.22	O3N2
SN2018ddr	IIb	UGC 8896	0.0146	69.2	83.7	8.44(+0.09/−0.09)	8.48	O3N2
SN2018gjx	IIb	NGC 865	0.0100	159.3	90.0	–	8.54	O3N2
SN2019bao	IIb	UGC 5687	0.0119	111.4	80.0	8.28(+0.15/−0.15)	8.38	O3N2
SN2019pqo	IIb	NGC 5980	0.0141	14.5	76.4	8.58(+0.02/−0.02)	8.61	O3N2
SN2020fqv	IIb	NGC 4568	0.0075	–	–	–	8.57	O3N2
SN2021bxu	IIb	ESO 478-G6	0.0178	101.8	57.7	8.49(+0.03/−0.03)	8.54	O3N2
ASASSN-15ta	Ib	GALEXASC J202933.17−615703.5	0.0150	83.5	48.9	8.28(+0.12/−0.11)	8.27	O3N2

Table A1 *– continued*

Name	Type	Host galaxy	Redshift	PA (deg)	*i* (deg)	12 + log(O/H) grad. (dex)	12 + log(O/H) local (dex)	Calibration
ASASSN-16ff	Ib	ESO 218-G008	0.0087	28.4	90.0	–	8.14	O3N2
AT2015dd	Ib	NGC 5483	0.0060	18.9	26.3	8.48(+0.02/−0.02)	–	O3N2
Gaia15acs	Ib	PGC 65805	0.0200	62.8	90.0	–	8.52	O3N2
MASTEROT J120451.50+265946.6	Ib	NGC 4080	0.0019	121.1	75.6	8.47(+0.10/−0.10)	8.48	O3N2
PS15cer	Ib	NGC 7349	0.0150	165.2	76.3	8.43(+0.07/−0.07)	8.43	O3N2
PTF09dfk	Ib	Anonymous	0.0160	99.4	44.6	8.32(+0.07/−0.07)	8.27	O3N2
SN2004cc	Ib	NGC 4568	0.0075	28.6	67.5	8.50(+0.05/−0.05)	8.55	O3N2
SN2004dk	Ib	NGC 6118	0.0052	58.1	68.7	8.56(+0.02/−0.02)	8.50	O3N2
SN2006lc	Ib	SDSS J24424.36−000943.4	0.0161	66.1	51.8	8.56(+0.04/−0.04)	8.56	O3N2
SN2009iu	Ib	NGC 7329	0.0108	107.3	42.7	8.58(+0.12/−0.12)	–	O3N2
SN2012au	Ib	NGC 4790	0.0045	87.0	58.8	8.48(+0.01/−0.01)	8.46	O3N2
SN2014ge	Ib	NGC 4080	0.0019	121.1	75.6	8.43(+0.07/−0.07)	8.48	O3N2
SN2016ajo	Ib	UGC 11344	0.0160	162.8	64.9	8.32(+0.04/−0.04)	8.28	O3N2
SN2016cdd	Ib	ESO 218-G008	0.0087	28.4	90.0	–	8.12	O3N2
SN2017ewx	Ib	NGC 5418	0.0160	45.4	68.5	8.50(+0.06/−0.06)	–	O3N2
SN2019ehk	Ib	NGC 4321	0.0043	153.0	24.0	8.58(+0.03/−0.03)	8.46	O3N2
SN2019yvr	Ib	NGC 4666	0.0050	40.6	69.6	8.58(+0.01/−0.01)	8.48	O3N2
SN2020admc	Ib	ESO 320-G31	0.0100	144.7	90.0	–	8.53	O3N2
SN2020hvp	Ib	NGC 6118	0.0052	58.1	68.7	8.55(+0.08/−0.08)	8.56	O3N2
SN2021kos	Ib	IC 719	0.0061	52.4	90.0	–	8.54	O3N2
SN2023crx	Ib	NGC1602	0.0120	22.9	81.2	8.54(+0.07/−0.07)	8.45	O3N2
iPTF13bvn	Ib	NGC 5806	0.0045	171.8	60.4	8.52(+0.04/−0.03)	8.59	O3N2
ASASSN-15kj	Ic	ESO 297-G37	0.0185	63.4	90.0	–	8.48	O3N2
ASASSN-21vr	Ic	NGC 3256	0.0094	87.2	48.2	8.53(+0.00/−0.00)	8.52	O3N2
SN2002J	Ic	NGC 3464	0.0125	110.8	50.8	8.52(+0.06/−0.06)	8.55	O3N2
SN2002ao	Ic	UGC 9299	0.0051	29.8	24.7	8.26(+0.09/−0.08)	8.37	O3N2
SN2005lr	Ic	ESO 492-G2	0.0086	153.6	48.8	8.49(+0.10/−0.10)	–	O3N2
SN2007rz	Ic	NGC 1590	0.0130	110.0	27.9	8.61(+0.03/−0.03)	8.62	O3N2
SN2009dt	Ic	IC 5169	0.0104	24.1	84.0	8.58(+0.04/−0.04)	8.57	O3N2
SN2010do	Ic	NGC 5374	0.0146	45.0	36.9	8.53(+0.02/−0.02)	8.58	O3N2
SN2011N	Ic	ESO 120-G16	0.0114	0.6	77.4	8.50(+0.05/−0.05)	8.53	O3N2
SN2011jm	Ic	NGC 4809	0.0031	65.0	90.0	–	8.14	O3N2
SN2013dk	Ic	NGC 4038	0.0055	160.4	51.9	8.54(+0.00/−0.00)	8.57	O3N2
SN2014L	Ic	NGC 4254	0.0080	60.0	20.1	8.60(+0.01/−0.01)	8.61	O3N2
SN2014eh	Ic	NGC 6907	0.0106	57.7	37.5	8.50(+0.05/−0.05)	8.41	O3N2
SN2016iae	Ic	NGC 1532	0.0040	34.2	83.0	8.53(+0.07/−0.07)	8.53	O3N2
SN2017fwm	Ic	ESO 141-IG32	0.0160	178.8	41.9	8.53(+0.06/−0.06)	–	O3N2
SN2017rt	Ic	NGC 3836	0.0120	137.7	39.8	8.40(+0.02/−0.02)	8.40	O3N2
SN2019yz	Ic	UGC 9977	0.0064	79.5	90.0	–	8.33	O3N2
SN2020oi	Ic	MESSIER 100	0.0052	153.0	24.0	8.59(+0.01/−0.01)	8.59	O3N2
SN2021aexi	Ic	NGC 7771	0.0140	68.0	66.7	8.58(+0.04/−0.04)	8.56	O3N2
SN2021ocs	Ic	NGC 7828	0.0191	136.7	90.0	–	8.49	O3N2
SN2023bqj	Ic	ESO-163-G011	0.0090	3.3	70.9	8.48(+0.18/−0.18)	8.49	O3N2
SN2023cj	Ic	NGC5468	0.0095	109.2	21.1	8.31(+0.05/−0.05)	–	O3N2

This paper has been typeset from a TEX/LATEX file prepared by the author.